Large-Signal Stabilization of Interleaved Multilevel Boost Converter Interfaced High-Power DC Microgrid Using an Adaptive Observer-Based Nonlinear Control Scheme

Wentao Jiang, *Member, IEEE*, Zhishuang Wang, Xiangke Li, *Member, IEEE*, Rui Ma, *Member, IEEE*, Sunhua Huang, Chaoyu Dong, and Xiaohua Wu

***Abstract*—The features of low current ripple and high voltage gain make the interleaved multilevel boost converter (IMBC) a promising topology to link low-voltage and high-power energy sources and the dc bus of the microgrid (MG). Considering the modern dc MG is highly penetrated by the constant power loads that threaten the system stability, a large-signal stabilization scheme for the IMBC-based dc MG is proposed in this article. An adaptive sliding mode observer (ASMO) is developed to estimate both matched and mismatched disturbances and, further, improve the control performance. Since the knowledge of the bounds of the disturbances and their derivatives is not required in the ASMO, a wide range of disturbances can be estimated. In addition, a unified reduced-order state–space model of the IMBC is derived to facilitate the design of the proposed control law. Moreover, a novel phase current balancing compensator is designed to balance the input phase currents of the IMBC. Finally, simulation and experimental results are demonstrated to show the effectiveness of the proposed method.**

***Index Terms*—Constant power load (CPL), dc microgrid (MG), disturbance observer, interleaved multilevel boost converter (IMBC), large-signal stabilization, sliding-mode control (SMC).**

I. Introduction

With the developments of renewable energy sources (RESs) and energy storage systems (ESSs), the dc microgrid (MG), which is one of the effective platforms to interface these sources and various loads, has drawn great interest. Considering the low and varying terminal voltage features in the RESs and ESSs, those sources are not suitable to link the dc MG directly [1]. To fill this gap, the boost-type converter is generally used to interface the sources to the dc bus of the MG.

The traditional boost converter (TBC) is an effective solution in many cases. However, due to the evitable parasitic elements in practice, its actual voltage gain is limited. Moreover, the drawback of high current ripple makes the TBC unsuitable for some sources, such as the fuel cell and battery [2]. In addition, the inductor current saturation problem prevents the utilization of TBC in high-power applications. To overcome the drawbacks of the TBC, an interleaved multilevel boost converter (IMBC) has been proposed [3]. Thanks to the combination of the interleaved structure (IS) and the Cockcroft Walton voltage multiplier (CWVM), the IMBC possesses the advantages of both the traditional interleaved boost converter [4] and multilevel boost converter (MBC) [5]. Specifically, the TIBC part allows the IMBC to operate in a low input current ripple and a high input current saturation boundary, and the MBC part provides the IMBC with a high stepup gain, self-voltage balancing feature, and low component voltage stress. Considering the numerous merits above-mentioned, in this article, the IMBC is selected as the interface converter for DGs, RESs, and ESSs in the dc MG.

With the penetration of power electronic devices into the modern dc MG, there exist many active loads, such as the motor driver and the converter-based appliances, that behave as constant power loads (CPLs) when they are tightly regulated. As the name suggested, the CPL consumes constant power with any dc bus voltage level. Hence, in the view of dc MG, the CPL shows the features of negative incremental impedance and high nonlinearity, which significantly threatens the system stability [6]. In addition, considering the high bandwidth of the CPL, the potential speedy and large CPL power changes introduce large-signal disturbances into the system, which further challenges the system's stabilization. Therefore, to alleviate the negative impacts of the CPLs on the dc MG and guarantee the system stability, the control schemes for the source side interfacing converters, such as the IMBC, are necessary to be designed.

Manuscript received 10 January 2024; accepted 23 February 2024. Date of publication 25 March 2024; date of current version 16 May 2024. This work was supported by the National Natural Science Foundation of China under Grant 52207224. Recommended for publication by Associate Editor S. Lukic. *(Corresponding author: Xiangke Li.)*

Wentao Jiang, Xiangke Li, Rui Ma, and Xiaohua Wu are with the Department of Electrical Engineering, Northwestern Polytechnical University, Xi'an 710072, China (e-mail: ewtjiang@nwpu.edu.cn; lixiangke@nwpu.edu.cn; rui.ma@nwpu.edu.cn; wxh@nwpu.edu.cn).

Zhishuang Wang is with the State Grid Tianjin Electric Power Research Institute, Tianjin 300380, China (e-mail: ezswang@163.com).

Sunhua Huang is with the Department of Electrical and Electric Engineering, Hong Kong Polytechnic University, Hong Kong 999077, China (e-mail: sunhua.huang@polyu.edu.hk).

Chaoyu Dong is with the Agency for Science, Technology and Research, Nanyang Technological University, Singapore 639798 (e-mail: dong0120@e.ntu.edu.sg).

Color versions of one or more figures in this article are available at https://doi.org/10.1109/TPEL.2024.3381158.

Digital Object Identifier 10.1109/TPEL.2024.3381158

Passive damping approaches have been widely adopted to stabilize the CPL-fed systems. Specifically, these approaches directly use extra passive components, such as resistors [7], capacitors [8], or *LC* filters [9], to increase the system damping. However, the extra physical elements result in additional weight, losses, and costs. Furthermore, the damping is usually limited by physical constraints. To increase the system damping without using the physical circuits, the active damping methods have been proposed [10], [11], [12]. In Lu et al.'s work [10], the virtual impedance is introduced into the dc MG system to maintain the system poles in the stable region. However, the additional impedance deteriorates the load performance. A virtual–resistor-based robust control method has been reported in Narm et al.'s work [11]. Although the dc MG system can be stabilized in a simple way, the resulting dc bus voltage deviation is not expected. In Zhang et al.'s work [12], a source-side series virtual impedance injection method has been presented. By establishing an equivalent source-side impedance, the desired stability margin can be achieved without degrading the performance of the CPLs. It is worth noting that both the passive and active damping methods are designed on the small-signal model of the system, which only ensures the system stability in a small neighborhood of a predefined system operation point. Hence, the actual operation point may be drawn out of this stability region by the large-signal disturbances, such as the frequent RES fluctuations and high amplitude of load power variations, thereby destroying the system stability.

To fill the gaps of the small-signal-based methods, the large-signal-based methods considering the intrinsic nonlinearity of the system with CPLs have been reported in many previous works. A passivity-based controller with a complementary proportional–integral (PI) controller has been proposed to regulate the dc–dc boost converter feeds CPLs [13]. However, the controller design demands an accurate system model for achieving satisfactory tracking performance and transient responses. In [14] and [15], the MPC technique is adopted for the dc MGs with CPLs. Although the expected control performance is achieved, the online computation efforts will grow exponentially with the expansion of the system scale, which results in heavy computational burdens. A robust sliding mode control (SMC) for a conventional dc–dc boost converter with the CPL has been proposed in Singh et al.'s work [16]. Since the controller design is based on a constant input side voltage, the control performance is sensitive to input voltage disturbances, which are unsuitable for RES-based applications. In Peng et al.'s work [17], the mixed potential theory is adopted to address the large-signal stability criterion of the parallel-connected dc–dc converters. The derived stability criterion helps the selection of circuit parameters and controller gains. However, the used simplified model is a linearized system, which degrades its effectiveness on other converters. Recently, some nonlinear disturbance observer-based backstepping control strategies have been proposed to stabilize the dc MG system with CPLs [18], [19]. In these strategies, the bounds of the disturbances and their derivatives are assumed to be known to design the controller, which limits their practical applications. In Wang et al.'s work [20], a high-order sliding mode observer is adopted to estimate the disturbance in a finite time, which improves the dynamic performance of the regulated dc MG system. Nevertheless, the information of the disturbances and their ith ($i = 1,2,3,4$) time derivatives are also required. Moreover, the aforementioned large-signal-based methods are mainly employed for conventional buck or boost converters, the modeling processes and the corresponding large-signal-based control strategies for the dc MG interfaced with the complex converters, such as the IMBC, are rarely discussed.

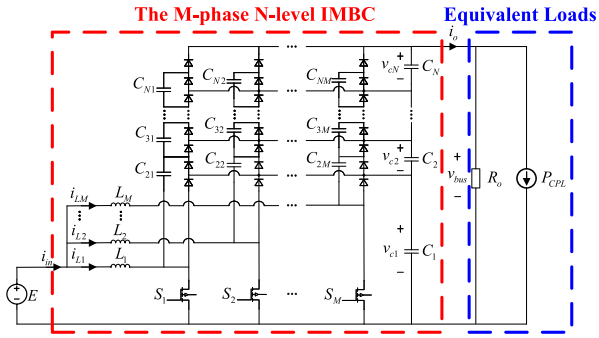

Fig. 1. Simplified DC MG fed by a M-phase N-level IMBC.

To fill gaps in existing works, in this article, a combined control strategy is proposed to stabilize the dc MG system interfaced by the IMBC. The main contribution of this article can be listed as follows.

1) A unified reduced-order model of the IMBC, which consists of the IS part and the CWVM part, has been derived. The structure and order of the proposed model are fixed, and they do not change with the changes in switched capacitor levels and interleave phases.
2) An adaptive sliding mode observer (ASMO)-based sliding mode control (SMC) strategy has been developed for the IMBC interfaced dc MG system to guarantee the system large-signal stability. Compared to some existing works [18], [19], [20], [21], [22], much wider ranges of disturbances can be handled by the proposed control strategy, which improves the robustness of the regulated system against the unknown disturbances.

In addition, a proportional–integral–resonance-based phase current balance compensator (PCBC) is added to keep interphase current equally sharing with eliminated oscillations caused by the weak sources and CPLs [30].

The rest of this article is organized as follows. In Section II, a generalized reduced-order model of the M-phase N-level IMBC is derived. The ASMO-based SMC is reported in Section III, and the corresponding large-signal stability analysis is addressed. In Sections IV and V, the simulation and experimental results are demonstrated, respectively. Finally, Section VI concludes this article.

II. Reduced-Order Model of the IMBC

To lower the analysis complexity, a simplified topology of the IMBC fed dc MG is deduced, as shown in Fig. 1. Note that the equivalent loads of the dc MG mainly contain resistive loads and the CPL. R_o and P_{CPL} represent the equivalent resistance

of lumped resistive loads and the equivalent power of the CPL, respectively.

A. Model Derivation

Before designing the controller for the IMBC, the corresponding mathematical converter model should be derived. Considering the high complexity and cascaded structure of the IMBC, the modeling process is carried out in two steps. First, using Kirchhoff's laws to analyze the M-phase interleaved network, the following averaged model can be obtained as:

$$\begin{cases} L_1 \frac{di_{L1}}{dt} = E - (1-d_1)v_{c1} \\ L_2 \frac{di_{L2}}{dt} = E - (1-d_2)v_{c1} \\ \quad \vdots \quad \vdots \quad \quad \vdots \\ L_M \frac{di_{LM}}{dt} = E - (1-d_M)v_{c1} \end{cases} \tag{1}$$

where M is the number of the inductors in the interleaved network, i_{Li} indicates the current passes the inductor of the ith phase, i.e., L_i $(i = 1, 2, \ldots, M)$, E denotes the nominal value of the input voltage, v_{c1} represents the voltage across the first output capacitor (C_1) of the voltage multiplier (VM) network, and d_i is the duty ratio of each the ith phase.

Assuming each inductor shares the same inductance L and the PWM switching signal of each phase is generated using the same duty ratio d with expected phase shifts, the model given in (1) can be simplified as

$$L_{\text{eq}} \frac{di_{\text{in}}}{dt} = E - (1-d)v_{c1} \tag{2}$$

where $i_{\text{in}} = \sum_{i=1}^{M} i_{Li}$ is the total input current and $L_{\text{eq}} = L/M$ is the equivalent input inductance.

According to (2), the M-phase interleaved network can be equivalent to a single-phase network with the input inductance of L_{eq}. Hence, using (2) and the VM network model reported in Villarreal-Hernandez et al.'s work [23] yields a generalized reduced-order model of the IMBC

$$\begin{aligned} L_{\text{eq}} \frac{di_{\text{in}}}{dt} &= E - (1-d)\frac{v_{\text{bus}}}{N} \\ C_{\text{eq}} \frac{dv_{\text{bus}}}{dt} &= (1-d)i_{\text{in}} - Ni_o \\ i_o &= \frac{v_{\text{bus}}}{R_0} + \frac{P_{\text{CPL}}}{v_{\text{bus}}}, C_{\text{eq}} = \frac{N + M(N-1)}{N}C \end{aligned} \tag{3}$$

where i_o is the output current, $v_{\text{bus}} = \sum_{i=1}^{N} v_{cj} = Nv_{c1}$ denotes the dc bus voltage, and C indicates the capacitance of each capacitor in the N-level VM network (all the capacitors are in the same capacitance).

B. Model Validation

To verify the accuracy of the proposed generalized model, both the frequency-domain and time-domain validations are carried out in this section. Two different parameter sets are used in the validations, and the details of system parameters are listed in Table I.

1) Time-Domain Validation: To validate the large-signal accuracy of the proposed model (3), some simulations with $\pm 10\%$ duty ratio step changes have been conducted using the MATLAB/Simulink. Fig. 2(a) and (b) shows the dynamic output voltage responses of the IMBC using the parameter Set 1 and Set 2, respectively, where the blue dotted wave indicates the response obtained using the proposed model and the red solid wave is the response obtained using the simulated circuit. As seen from the figures, good matches are achieved between the proposed generalized model and the simulated IMBC circuit in time-domain for various sets of system parameters.

TABLE I
PARAMETERS FOR MODEL VALIDATION

Description	Symbol	Value (Set 1)	Value (Set 2)
Switching frequency	f_s	20 kHz	20 kHz
Number of level	N	3	2
Number of phase	M	3	2
Nominal input voltage	E	100 V	100 V
Nominal dc bus voltage	$V_{\text{bus}}^{\text{ref}}$	600 V	400 V
Inductance	L	330 μH	360 μH
Capacitance	C	470 μF	470 μF
Resistive load	R_o	10 Ω	10 Ω
CPL	P_{CPL}	5.0 kW	5.0 kW

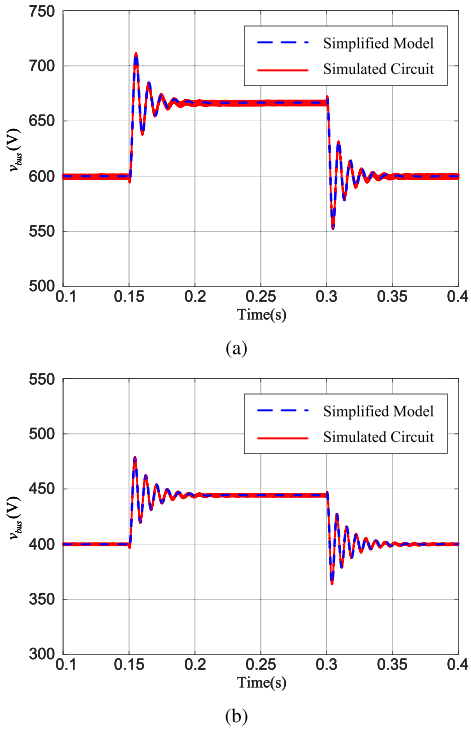

Fig. 2. Output voltage dynamic responses for $\pm 10\%$ duty ratio step changes of the IMBC with (a) parameter Set 1 and (b) parameter Set 2.

2) Frequency-Domain Validation: To validate the small-signal accuracy of the proposed model in frequency-domain, the transfer function between the duty ratio d and the output voltage v_{bus} is derived and given as

$$\begin{aligned} G_{vd}(s) &= \frac{\tilde{v}_{\text{bus}}}{\tilde{d}} = \frac{a_1 s + a_0}{b_2 s^2 + b_1 s + b_0} \\ a_0 &= -E^2 R_o \left(V_{\text{bus}}^{\text{ref}}\right)^2 \left[P_{\text{CPL}} R_o - \left(V_{\text{bus}}^{\text{ref}}\right)^2\right] \end{aligned}$$

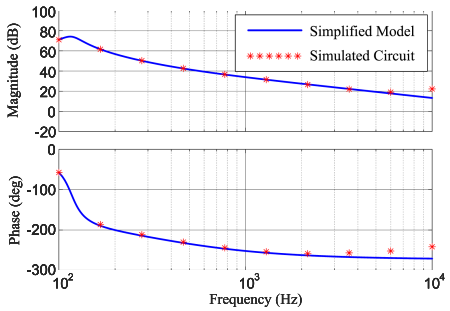

(a)

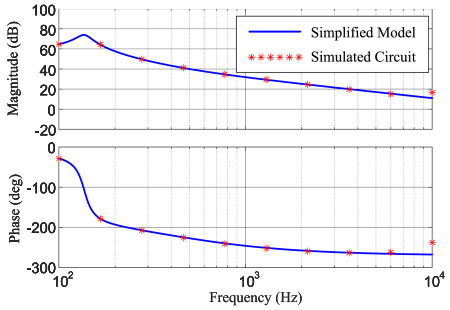

(b)

Fig. 3. Frequency-domain responses of the IMBC with (a) parameter Set 1 and (b) parameter Set 2 (dotted star curve obtained from the simulated IMBC circuit; solid blue curve obtained from the (4).

$$
\begin{aligned}
a_1 &= L_{\rm eq}\left(V_{\rm bus}^{\rm ref}\right)^2\left[(P_{\rm CPL}R_o)^2-\left(V_{\rm bus}^{\rm ref}\right)^4\right]\\
b_0 &= NR_oE^3\left[\left(V_{\rm bus}^{\rm ref}\right)^2-P_{\rm CPL}R_o\right]\\
b_1 &= L_{\rm eq}NER_o^2\left(V_{\rm bus}^{\rm ref}\right)^4\\
b_2 &= C_{\rm eq}L_{\rm eq}ER_o\left(V_{\rm bus}^{\rm ref}\right)^2\left[P_{\rm CPL}R_o-\left(V_{\rm bus}^{\rm ref}\right)^2\right]
\end{aligned}
\tag{4}
$$

where the symbols with the tilde "˜" denote the small-signal perturbations.

Then, using the circuit parameters given in Table I, the bode plots of both (4) and the corresponding simulated circuit (established in MATLAB/Simulink) can be obtained as shown in Fig. 3. Specifically, Fig. 3(a) and (b) is plotted using parameter Set 1 and Set 2, respectively. It can be seen from both figures that, the frequency responses of the proposed model are in good agreement with those of the simulated electric circuit up to half of the switching frequency (10 kHz) for both sets of system parameters. Based on the validation results obtained from both time-domain and frequency domain, the proposed generalized reduced-order model has a high accuracy, which is available for the controller design and system analysis on the M-phase N-Level IMBC system.

In practice, the deviations in the inductance and capacitance are unavoidable, and the terminal voltage of the input source may also differ from its nominal value (such as the battery operates with a low state-of-charge). Hence, without losing the generality, the reduced-order model given in (3) can be rewritten as

$$
(L_{\rm eq}+\Delta L)\frac{di_{\rm in}}{dt}=(E+\Delta E)-(1-d)\frac{v_{\rm bus}}{N}
$$

$$
(C_{\rm eq}+\Delta C)\frac{dv_{\rm bus}}{dt}=(1-d)i_{\rm in}-Ni_o \tag{5}
$$

where ΔL and ΔC are the equivalent uncertainties in inductance and capacitance, respectively; ΔE represents the unknown deviation in the input source terminal voltage.

Note that, in this article, only the nominal values of the circuit parameters, such as L, C, and E, are known. The deviations between actual values and nominal values are treated as unknown uncertainties.

III. SMC Design

In this section, an adaptive ASMO-based SMC algorithm is designed for the IMBC with CPL. The main control objective is to let the dc bus voltage $v_{\rm bus}$ tightly track its reference $v_{\rm bus}^{\rm ref}$ without the steady-state error even in the presence of large-signal disturbances.

A. Model Transformation

Although the reduced-order model of the IMBC is derived, the intrinsic nonlinear feature is still not friendly to the controller design. Referring to Sira-Ramirez and Ilic-Spong's work [24] and considering the stored energy and input power of the IMBC, the original nonlinear model (3) can be transformed to a canonical linear form of (7) by using the following new state variables:

$$
\begin{cases}
x_1=\frac{1}{2}L_{\rm eq}i_{\rm in}^2+\frac{1}{2}HC(\frac{v_{\rm bus}}{N})^2\\
x_2=Ei_{\rm in}
\end{cases}
\tag{6}
$$

where x_1 represents the nominal value of the total energies stored in the IMBC, x_2 indicates the converter input power and $H=N+M(N-1)$.

Based on (5) and (6), the time derivatives of the new state variables can be calculated as

$$
\begin{aligned}
\dot{x}_1 &= x_2+u_1\\
\dot{x}_2 &= v+u_2
\end{aligned}
\tag{7}
$$

where the v indicates the intermediate control law, and u_1 and u_2 are unmeasurable disturbances. The corresponding expressions are given as

$$
\begin{aligned}
v &= \frac{E}{L_{\rm eq}}\left[E-(1-d)\frac{v_{\rm bus}}{N}\right]\\
u_1 &= (-v_{\rm bus}i_o+i_{\rm in}\Delta E)-\frac{\Delta Cv_{\rm bus}}{(C_{\rm eq}+\Delta C)N}\left[i_{\rm in}(1-d)-Ni_o\right]\\
&\quad-\frac{\Delta Li_{\rm in}}{L_{\rm eq}+\Delta L}\left[E+\Delta E-(1-d)\frac{v_{\rm bus}}{N}\right]\\
u_2 &= \frac{L_{\rm eq}E\Delta E-E\Delta L[E-(1-d)\frac{v_{\rm bus}}{N}]}{L_{\rm eq}(L_{\rm eq}+\Delta L)}.
\end{aligned}
\tag{8}
$$

Herein, d is treated as the actual control law, which can be derived as

$$
d=1-\frac{NE}{v_{\rm bus}}+\frac{NL_{\rm eq}v}{Ev_{\rm bus}}. \tag{9}
$$

It is worth mentioning that, in this article, the term "disturbances" is not limited to the disturbances caused by external

impacts, circuit uncertainties, and so on. It is similar to the concept of "total disturbance" proposed by Han [25], which is a multivariable function containing system states, uncertainties, unmeasurable parameters, and external disturbances.

After the model transformation, the reduced-order model (5) is equivalent to its diffeomorphism (7), and hereafter, the control objective is changed to regulate the total stored energy x_1 track its reference x_1^{ref} asymptotically.

According to (6), x_1^{ref} and x_2^{ref} can be identified as

$$x_1^{\text{ref}} = \frac{1}{2}L_{\text{eq}}(I_{\text{in}}^{\text{ref}})^2 + \frac{1}{2}HC\left(\frac{V_{\text{bus}}^{\text{ref}}}{N}\right)^2 \tag{10}$$

$$x_2^{\text{ref}} = EI_{\text{in}}^{\text{ref}} \tag{11}$$

assuming the power loss of the IMBC is negligible, based on the principle of input/output power balance, the following relationship can be held:

$$i_{\text{in}}(E+\Delta E) = P_{\text{out}} \tag{12}$$

where P_{out} indicates the converter total output power.

Based on (12), the reference of the total input current i_{in} can be defined as

$$I_{\text{in}}^{\text{ref}} = \frac{P_{\text{out}} - i_{\text{in}}\Delta E}{E}. \tag{13}$$

In addition, at steady-state, the following relationships involve the dynamics listed in (5) can be obtained:

$$\begin{aligned}\left[(L_{\text{eq}}+\Delta L)\frac{di_{\text{in}}}{dt}\right]_{ss} &= E+\Delta E-(1-d)\frac{v_{\text{bus}}}{N} = 0\\ \left[(C_{\text{eq}}+\Delta C)\frac{dv_{\text{bus}}}{dt}\right]_{ss} &= (1-d)i_{\text{in}} - Ni_o = 0.\end{aligned} \tag{14}$$

Substituting (14) into (8), disturbance u_1 at steady-state can be expressed as

$$u_{1ss} = -v_{\text{bus}}i_o + i_{\text{in}}\Delta E = i_{\text{in}}\Delta E - P_{\text{out}}. \tag{15}$$

Now, using (12)–(15), the references of x_1 and x_2 [given in (10) and (11)] can be rewritten as

$$x_1^{\text{ref}} = \frac{1}{2}L_{\text{eq}}\left(\frac{-u_{1ss}}{E}\right)^2 + \frac{1}{2}HC\left(\frac{V_{\text{bus}}^{\text{ref}}}{N}\right)^2 \tag{16}$$

$$x_2^{\text{ref}} = -u_{1ss}. \tag{17}$$

B. Adaptive Sliding-Mode Observer

According to (7), the disturbances u_1 and u_2 deteriorate both the dynamic and steady-state performance of the studied system, and their unmeasurable features make such impacts hard to be eliminated only using the feedback control law. To fill this gap, an ASMO is designed in this section, which can compensate for the disturbance impacts in a feedforward manner.

Considering both u_1 and u_2 mainly consist of physical circuit parameter deviations and the input/output power of the IMBC, it is reasonable to make the following assumption.

Assumption 1: The first and second order time derivatives of the disturbance $u_i(t)$ satisfied

$$\sup_{t>0}|\dot{u}_i(t)| < \Gamma_{i1}, \sup_{t>0}|\ddot{u}_i(t)| < \Gamma_{i2} \tag{18}$$

where the upper bounds Γ_{i1} and Γ_{i2} are unknown positive constants, and only the order of Γ_{i2} is known. Noted that the bounds of the disturbances are not necessary for the observer design, which includes a wider range of disturbances compared to several existing works [18], [19], [20], [21], [22].

Defining the following variables:

$$\begin{cases}\zeta_{u1} = \hat{x}_1 - x_1\\ \zeta_{u2} = \hat{x}_2 - x_2\\ \dot{\hat{x}}_1 = x_2 - h_{u1}\text{sgn}(\zeta_{u1})|\zeta_{u1}|^{\lambda_{u1}} + \hat{u}_1\\ \dot{\hat{x}}_2 = v - h_{u2}\text{sgn}(\zeta_{u2})|\zeta_{u2}|^{\lambda_{u2}} + \hat{u}_2\end{cases} \tag{19}$$

where $\hat{x}_i$ and $\hat{u}_i$ $(i=1,2)$ are the estimations of the x_i and u_i, respectively; h_{ui} and λ_{ui} $(i=1,2)$ are positive constants, and $0<\lambda_{ui}<1$.

Using the variables defined in (19), the ASMO to estimate the disturbance u_i is designed as

$$\begin{cases}s_{ui} = \dot{\zeta}_{ui} + h_{ui}\text{sgn}(\zeta_{ui})|\zeta_{ui}|^{\lambda_{ui}}\\ \dot{\hat{u}}_i = -(k_{ui}+\gamma_{ui})\,\text{sgn}(s_{ui})\end{cases} \tag{20}$$

with the following adaptive gains:

$$\begin{aligned}\dot{k}_{ui} &= -\rho_{ui}\text{sgn}(\sigma_{ui})\\ \dot{\alpha}_{ui} &= \begin{cases}\eta_{ui}|\sigma_{ui}| & ,\text{when } |\sigma_{ui}| > \sigma_{0ui}\\ 0 & ,\text{when } |\sigma_{ui}| \le \sigma_{0ui}\end{cases}\end{aligned} \tag{21}$$

where

$$\begin{aligned}\rho_{ui} &= \alpha_{0ui} + \alpha_{ui}\\ \sigma_{ui} &= k_{ui} - \frac{1}{\beta_{ui}}|\phi_{ui}| - \varepsilon_{ui}\\ \dot{\phi}_{ui} &= \frac{1}{\tau_{ui}}\left[-(k_{ui}+\gamma_{ui})\,\text{sgn}(s_{ui}) - \phi_{ui}\right].\end{aligned} \tag{22}$$

The $\text{sgn}(\bullet)$ indicates the signum function, and the observer gains β_{ui}, γ_{ui}, η_{ui}, σ_{0ui}, α_{0ui}, ε_{ui}, τ_{ui}, and l_{ui} are user-defined positive scalars.

Then, using (7) and (19), the proposed ASMO (20) can be rewritten as

$$\begin{cases}s_{ui} = \hat{u}_i - u_i\\ \dot{\hat{u}}_i = -(k_{ui}+\gamma_{ui})\,\text{sgn}(s_{ui}).\end{cases} \tag{23}$$

According to [26], under Assumption 1, $s_{ui}=0$ can be achieved in finite time if the observer gains are selected to satisfy the following conditions:

$$\begin{aligned}l_{ui} &> \sup\left(1, \frac{|\dot{\phi}_{ui}|}{\Gamma_{i2}}\right), 0<\beta_{ui}<1\\ \frac{\varepsilon_{ui}^2}{4} &> \sigma_{0ui}^2 + \frac{1}{\eta_{ui}}\left(\frac{l_{ui}\Gamma_{i2}}{\beta_{ui}}\right)^2\end{aligned} \tag{24}$$

where $\sup(\bullet)$ represents the supremum function.

Hence, based on (23) and (24), once the appropriate observer gains are selected, the disturbance estimation $\hat{u}_i$ will converge to u_i in a finite time, and the convergence time can be defined as T_{ob}.

C. Controller Design

Since the disturbance u_1 is not available in many practical scenarios without using extra sensors, the exact value of the state variable references given in (16) and (17) are hard to obtain directly. Based on the conclusion drawn in the previous section, $\hat{u}_i$ is able to converge to u_i within a finite time T_{ob}. Therefore, the following equations can be achieved at steady-state:

$$\hat{u}_1 = u_{1ss} \text{ and } \hat{u}_2 = u_{2ss}. \tag{25}$$

Then, it is reasonable to use the estimated state variable references, which are given as (26) and (27), to establish the control law

$$\hat{x}_1^{\text{ref}} = \frac{1}{2}L_{\text{eq}}\left(\frac{-\hat{u}_1}{E}\right)^2 + \frac{1}{2}HC\left(\frac{V_{\text{bus}}^{\text{ref}}}{N}\right)^2 \tag{26}$$

$$\hat{x}_2^{\text{ref}} = -\hat{u}_1. \tag{27}$$

Using (26) and (27), the state error variables are defined as

$$e_{x1} = x_1 - \hat{x}_1^{\text{ref}} \tag{28}$$

$$e_{x2} = x_2 - \hat{x}_2^{\text{ref}}. \tag{29}$$

Considering (7), (28), and (29), a sliding surface is designed as

$$s_x = a_x e_{x1} + e_{x2} \tag{30}$$

where a_x is a positive constant.

To achieve the expected sliding motion, an SMC law using the estimations from ASMO is given as

$$\begin{aligned} v = & -a_x(e_{x2} - \dot{\hat{x}}_1^{\text{ref}}) - \dot{\hat{u}}_1 - \hat{u}_2 \\ & - K_{s1}\text{sgn}(s_x) - K_{s2}s_x \end{aligned} \tag{31}$$

where K_{s1} and K_{s2} are positive SMC gains to be designed.

D. Large-Signal Stability Analysis

Considering the proposed ASMO-based SMC given in (20), (30), and (31), the main proposition of this article is given as follows.

Proposition 1: Based on Assumption 1, once the inequalities given in (24) are held and the SMC gains $K_{s1} > 0$, $K_{s2} > 0$, and $a_x > 0$ are selected, the studied M-phase and N-level IMBC system regulated by the SMC law given in (31) is asymptotically stable, and the dc bus voltage v_{bus} converges to V_{bus}^{ref} asymptotically.

Proof: Considering the finite-time convergence feature of the ASMO, the proof is carried out in two steps. During $t < T_{\text{ob}}$, the disturbance observing errors e_{u1} and e_{u2} do not converge to zero, and the corresponding dynamics of the regulated system can be expressed as

$$\begin{cases} \dot{e}_{x1} = e_{x2} + e_{u1} - \dot{\hat{x}}_1^{\text{ref}} \\ \dot{e}_{x2} = -a_x\left(e_{x2} - \dot{\hat{x}}_1^{\text{ref}}\right) - K_{s1}\text{sgn}(s_x) \\ \qquad\qquad -K_{s2}s_x + e_{u2} \\ \dot{s}_x = a_x e_{u1} + e_{u2} - K_{s1}\text{sgn}(s_x) - K_{s2}s_x. \end{cases} \tag{32}$$

A finite-time bounded function is defined as [27]

$$V_{\text{bf}}(e_{x1}, e_{x2}, s_x) = \frac{1}{2}\left(e_{x1}^2 + e_{x2}^2 + s_x^2\right). \tag{33}$$

Based on (32), the time derivative of V_{bf} is derived as

$$\begin{aligned} \dot{V}_{\text{bf}} &= \dot{e}_{x1}e_{x1} + \dot{e}_{x2}e_{x2} + \dot{s}_x s_x \\ &= e_{x1}e_{x2} + e_{x1}e_{u1} - e_{x1}\dot{\hat{x}}_1^{\text{ref}} - a_x e_{x2}^2 + e_{x2}e_{u2} \\ &\quad + a_x e_{x2}\dot{\hat{x}}_1^{\text{ref}} - K_{s1}e_{x2}\text{sgn}(s_x) - K_{s2}e_{x2}s_x \\ &\quad + a_x e_{u1}s_x + e_{u2}s_x - K_{s1}|s_x| - K_{s2}s_x^2 \\ &\le |e_{x1}e_{x2}| + |e_{x1}e_{u1}| + |e_{x1}\dot{\hat{x}}_1^{\text{ref}}| + |e_{x2}e_{u2}| \\ &\quad + a_x|e_{x2}\dot{\hat{x}}_1^{\text{ref}}| + K_{s1}|e_{x2}| + K_{s2}|e_{x2}s_x| \\ &\quad + a_x|e_{u1}s_x| + |e_{u2}s_x|. \end{aligned} \tag{34}$$

Using Young's inequality on (34) yields

$$\begin{aligned} \dot{V}_{\text{bf}} &\le \frac{1}{2}\left(e_{x1}^2 + e_{x2}^2\right) + \frac{1}{2}\left(e_{x1}^2 + e_{u1}^2\right) + \frac{1}{2}\left(e_{x2}^2 + e_{u2}^2\right) \\ &\quad + \frac{1}{2}\left[e_{x1}^2 + (\dot{\hat{x}}_1^{\text{ref}})^2\right] + \frac{a_x}{2}\left[e_{x2}^2 + (\dot{\hat{x}}_1^{\text{ref}})^2\right] \\ &\quad + \frac{K_{s1}}{2}\left(1 + e_{x2}^2\right) + \frac{K_{s2}}{2}\left(e_{x2}^2 + s_x^2\right) \\ &\quad + \frac{a_x}{2}\left(e_{u1}^2 + s_x^2\right) + \frac{1}{2}\left(e_{u2}^2 + s_x^2\right) \\ &\le K_{\text{bf}}V_{\text{bf}} + \Psi_{\text{bf}} \end{aligned} \tag{35}$$

where

$$K_{\text{bf}} = \max\{3, 2 + a_x + K_{s1} + K_{s2}\}$$

$$\Psi_{\text{bf}} = \frac{1}{2}\left[a_x e_{u1}^2 + 2e_{u2}^2 + (1 + a_x)(\dot{\hat{x}}_1^{\text{ref}})^2 + K_{s1}\right].$$

Since all the elements consist of K_{bf} and Φ_{bf} are bounded, the finite-time bounded function V_{bf} will not escape in finite-time, and hence, e_{x1}, e_{x2}, and s_x are bounded during $t < T_{\text{ob}}$ [28].

Once $t \ge T_{\text{ob}}$, the disturbance observing errors e_{u1} and e_{u2} converge to zero. The resulting dynamic of the sliding variable s_x is given as

$$\dot{s}_x = -K_{s1}\text{sgn}(s_x) - K_{s2}s_x. \tag{36}$$

Defining a candidate Lyapunov function as

$$V_{sx} = \frac{1}{2}s_x^2. \tag{37}$$

Taking the time derivative of V_{sx} yields

$$\dot{V}_{sx} = -K_{s1}|s_x| - K_{s2}s_x^2 \tag{38}$$

which implies the sliding variable $s_x = 0$ can be achieved in a finite time.

Based on (30), $s_x = 0$ results in

$$e_{x2} = -a_x e_{x1}. \tag{39}$$

Then, using (28), (39), and $e_{u1} = 0$ yields

$$\dot{x}_1 = -a_x(x_1 - x_1^{\text{ref}}). \tag{40}$$

Solving (40) yields

$$x_1(t) = ce^{-a_x t} + x_1^{\text{ref}} \tag{41}$$

where c is constant. Hence, by appropriately selecting the ASMO and controller gains, the regulated system is asymptotically stable and v_{bus} converges to its reference $V_{\text{bus}}^{\text{ref}}$ asymptotically. The proof is completed. ■

E. Phase Current Balancing Compensator

In previous sections, the reduced-order model given in (5) is used to design the ASMO-based SMC. However, considering the circuit parameter and duty-ratio deviations in practice, the use of the total input current as the state variable may result in imbalance issues between the interphase currents, which increases the input current ripple and lowers the conversion efficiency [29]. To solve the issues, a simple but effective PCBC is adopted in the closed-loop IMBC system. The main control objective is to guarantee each interphase current shares the same value of $i_{\text{ave}} = i_{\text{in}}/M$.

Considering that CPLs may cause the low-frequency and subsynchronous oscillations in the dc MG system, the adopted PCBC is designed using both the PI and proportional–resonance techniques, which can be expressed as

$$d_i^{\text{com}} = \left(k_p + \frac{k_i}{s} + \frac{2k_{rs}\omega_c s}{s^2 + 2\omega_c s + \omega_o^2}\right) e_i^{\text{com}} \tag{42}$$

where $e_i^{\text{com}} = (i_{\text{ave}} - i_{Li})$; k_p, k_i, and k_{rs} are positive controller gains; ω_c and ω_o are the cutoff frequency and the resonance frequency, respectively. Note that the first two items are the PI part, which is in charge of controlling the dc component while the third item is the resonance part, which handles the low-frequency components.

According to Wang et al.'s work [30], the frequency of the oscillations caused by the weak sources and CPLs are generally lower than 5 Hz. Hence, it is reasonable to select $\omega_o = 18.85$ rad/s (around 3 Hz) which is a midpoint. The value of ω_c determines the width of the resonance frequency, in this article, it is selected as $\omega_c = 0.314$ rad/s (around 0.1 Hz). In addition, to avoid the controller interactivity, the values of k_p, k_i, and k_{rs} should be selected to guarantee the bandwidth of the PCBC is much lower than that of the proposed ASMO-based SMC.

Then, the final control law of each phase can be derived as

$$d_i = d + d_i^{\text{com}}, i = 1, 2, \ldots, M. \tag{43}$$

The overall block diagram of the proposed controller is given in Fig. 4.

IV. Simulation Results

Considering the numerous observer gains and control gains used in the proposed ASMO-based SMC, brief tuning guidelines of the critical gains are given to simplify the controller design. The effectiveness of the proposed controller against various types of large-signal disturbances is verified by corresponding cases. The circuit parameters used in this work are summarized in Table II. In addition, a comparative study involves a PI controller and the proposed controller is carried out to show the advantages of the latter in terms of the dc bus voltage stabilization. Without losing the generality, a three-phase and two-level IMBC is adopted for all simulations.

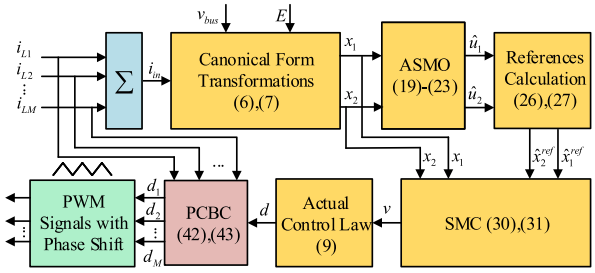

Fig. 4. Overall control diagram of the proposed strategy.

TABLE II
Simulation and Experimental Parameters

Description	Symbol	Values
Switching frequency	f_s	20 kHz
Input voltage	E	100 V
Nominal dc bus voltage	$v_{\text{bus}}^{\text{ref}}$	400 V
Interleaved inductor	$L_1/L_2/L_3$	1.0 mH
Multilevel capacitor	C_1/C_2	470 μF
CPL	P_{CPL}	2.0 kW

A. Parameter Tuning Guidelines

Since the proposed control scheme consists of the ASMO and the SMC, both the observer gains and controller gains impact the dynamic performance of the regulated system. The tuning guidelines of the observer gains are addressed first.

In the simulations, the system starts up with mixed loads, where the resistive load power $P_R = 1.6$ kW and the CPL power $P_{\text{CPL}} = 2$ kW. At $t = 0.015$ s, the resistive load is plugged out and the system operates with the pure CPL. At $t = 0.03$s, the power of CPL step changes from $P_{\text{CPL}} = 2$ kW to $P_{\text{CPL}} = 6$ kW. To figure out the impacts of the observer gains on the observing performance, in each simulation, only one gain is varying and others are fixed.

Assuming $\Delta E = 0$, according to (15), the negative value of the disturbance u_1 at steady-state is approximate to that of the output power P_{out}. Hence, the disturbance estimate $\hat{u}_1$ should converge to $-P_{\text{out}}$ at steady-state. Fig. 5(a) shows the dynamic responses of $\hat{u}_1$ with different h_{ui}. From the zoom-in figures, it can be seen that the lower h_{ui} results in a faster convergence rate of $\hat{u}_1$. Fig. 5(b) illustrates the dynamic responses of $\hat{u}_1$ with various α_{0ui}. It can be found that the greater α_{0ui} increases the convergence rate of $\hat{u}_1$. The dynamic responses of $\hat{u}_1$ with varying η_{ui} are given in Fig. 5(c). As seen from the figure, the value of η_{ui} significantly impacts the dynamic of $\hat{u}_1$. In detail, the larger value of η_{ui} provides $\hat{u}_1$ a shorter settling time. Fig. 5(d) shows the responses of $\hat{u}_1$ with various values of β_{ui}. Clearly, the increases of β_{ui} slow down the convergence of $\hat{u}_1$. The responses of $\hat{u}_1$ using various values of γ_{1_ui} and γ_{2_ui} are shown in Fig. 6(a) and (b), respectively. It can be obtained that $\gamma_{1_u i}$ has no distinct effect on the estimate dynamics while the greater $\gamma_{2_u i}$ results in a shorter converging period during startup.

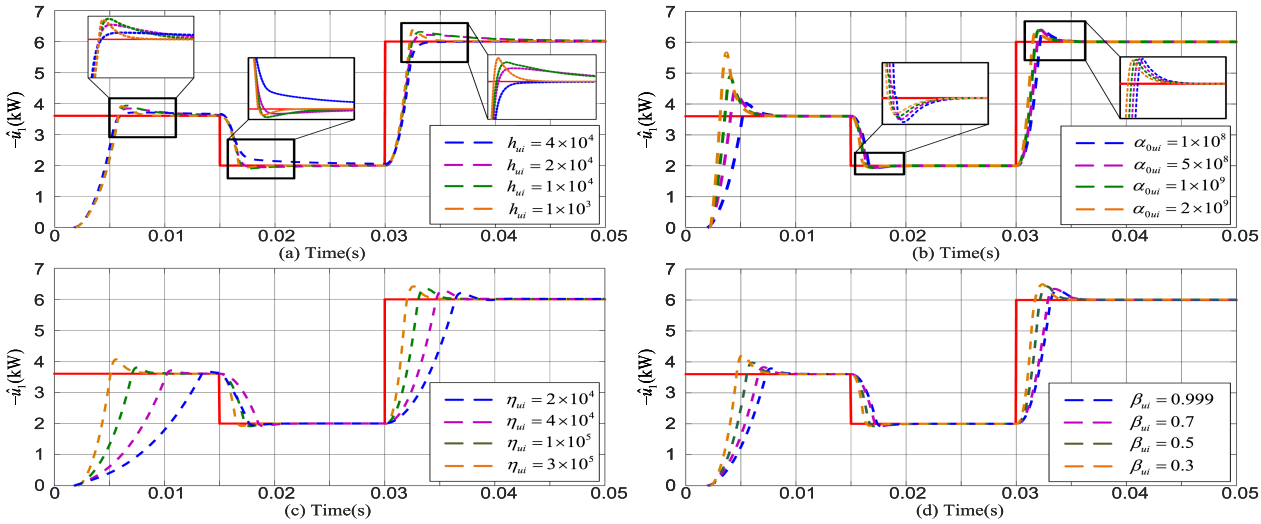

Fig. 5. Dynamic responses of the estimator $\hat{u}_1$ with various (a) h_{ui}, (b) α_{0ui}, (c) η_{ui}, (d) β_{ui}, $(i = 1, 2)$.

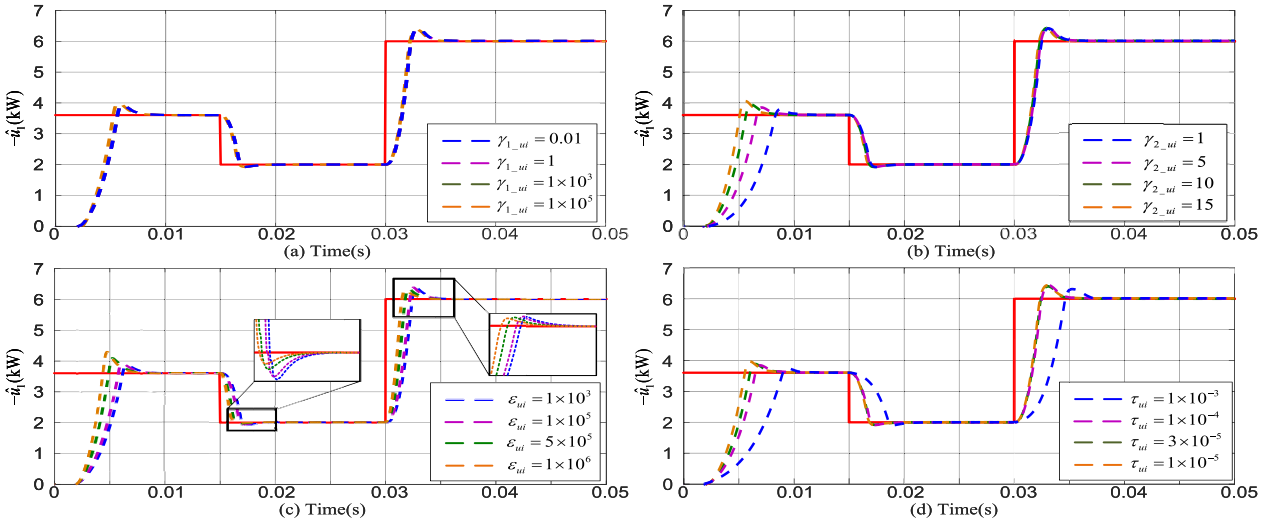

Fig. 6. Dynamic responses of the estimator $\hat{u}_1$ with various (a) γ_{1_ui}, (b) γ_{2_ui}, (c) ε_{ui}, (d) τ_{ui}, $(i = 1, 2)$.

Fig. 6(c) demonstrates the dynamics of $\hat{u}_1$ for the varying ε_{ui}. Similar to α_{0ui} and η_{ui}, the increments of ε_{ui} speed up the convergence of $\hat{u}_1$. In Fig. 6(d), the response waveforms of $\hat{u}_1$ with various τ_{ui} are shown. It can be seen that the smaller τ_{ui} leads to a shorter converging period of $\hat{u}_1$, especially in the startup stage. The dynamic responses of $\hat{u}_1$ with various λ_{ui} is given in Fig. 7. Obviously, the value of λ_{ui} has a negligible effect on the dynamic performance of the estimator.

Considering the simulation results shown in Figs. 5–7, the turning guidelines of the observer gains can be roughly given as follows.

1) Large values of α_{0ui}, η_{ui}, and ε_{ui} are suggested to be chosen to guarantee acceptable dynamic estimating performance during both the startup and power changing periods.
2) Small values of h_{ui} and β_{ui} should be selected to further improve the dynamic performance of the estimator.

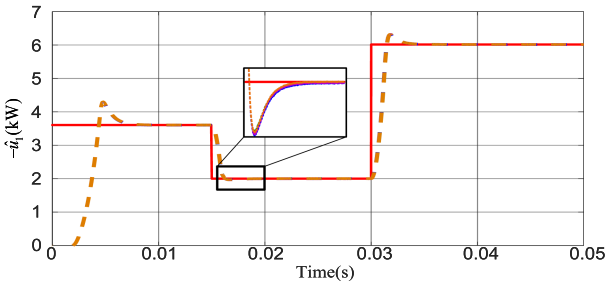

Fig. 7. Dynamic responses of the estimator $\hat{u}_1$ with various λ_{ui} $(i = 1, 2)$.

3) After determining the previous five parameters, a reasonably great γ_{2_ui} and a small τ_{ui} can be set to achieve a desired dynamic estimating response in the startup stage.
4) A small value of γ_{1ui} can be selected to alleviate the chattering problem caused by (20), and $0 < \lambda_{ui} < 1$

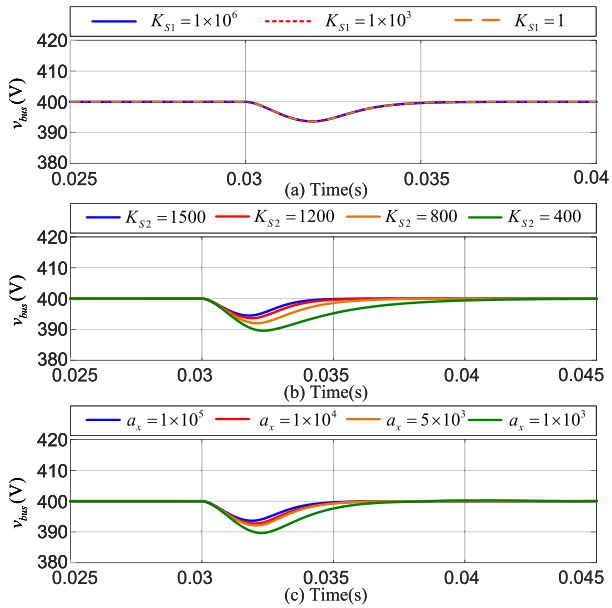

Fig. 8. Dynamic responses of the bus voltage $v_{\rm bus}$ with various (a) K_{s1}, (b) K_{s2}, (c) a_x.

should be chosen to guarantee the finite-time stable of ζ_{ui} [26].

Next, the selections of the controller gains are analyzed. Fig. 8 shows the dynamic responses of $v_{\rm bus}$ in the presence of CPL step changes (from 2 to 6 kW). Based on all three sub-figures, it can be obtained that choosing large values of K_{s2} and a_x provide a short settling time and a lower dip in the transient dc bus voltage. In addition, since K_{s1} has no obvious contribution to the transient response of $v_{\rm bus}$, a small K_{s1} should be selected to relieve the chattering problem caused by the SMC. Note that, to achieve the desired control performance, the bandwidth of the SMC is expected to be much slower than that of the ASMO.

B. Proposed Controller Verification

According to the tuning guidelines given previously, the appropriate ASMO gains and SMC gains can be selected. To simulate the worst stability condition, pure CPL is adopted for the following simulations. The corresponding simulation results of the closed-loop IMBC system in the presence of various disturbances are shown in the following.

1) CPL Variations: Fig. 9(a) shows transient responses in the presence of pure CPL changes. Specifically, $P_{\rm CPL}$ jumps from 2.0 to 6.0 kW at t = 0.05 s, and, then, drops to 4.0 kW at t =0.07 s. It can be noticed that the impacts of the CPL changes on the dc bus voltage are eliminated within 5.0 ms, and the interphase current balance and self-voltage balance are achieved well during the transients and steady states.

2) Input Voltage Variations: Fig. 9(b) shows transient responses of the studied system in the presence of input voltage changes. In detail, E drops from 100 to 60 V at t = 0.05 s and, then, increases to 80 V at t = 0.07 s. Again, the dc bus voltage is regulated to its reference with a short transient period (within 3.0 ms) and the interphase currents balance and the self-voltage balance through the switched-capacitor network are still achieved. It is worth noting that the voltage dips caused by E variations are negligibly small.

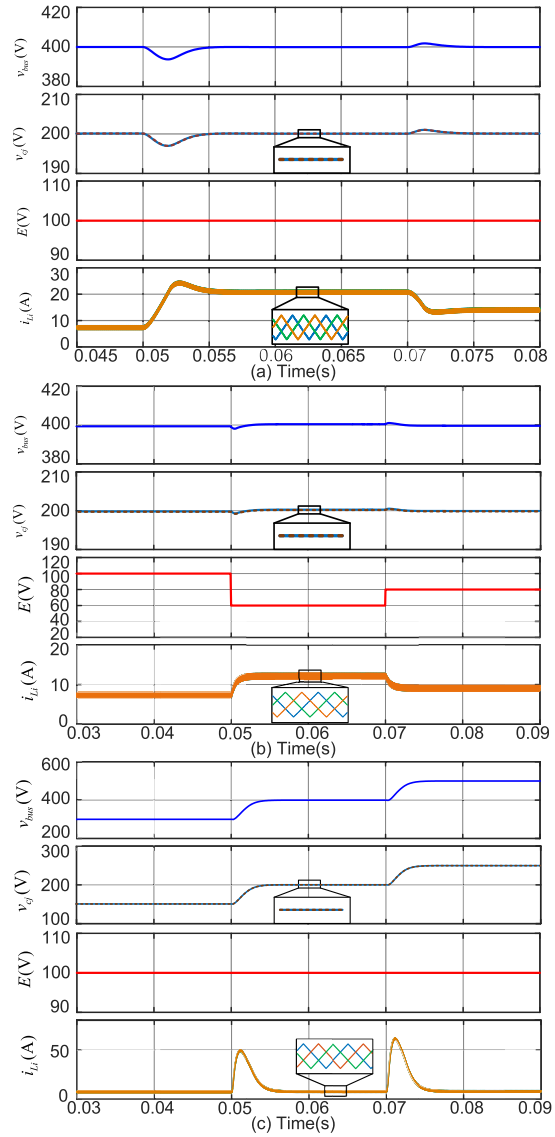

Fig. 9. Dynamic responses of the IMBC in the presence of (a) CPL variations, (b) input voltage variations, (c) output voltage reference variations.

3) Output Voltage Reference Variations: Fig. 9(c) shows transient responses of the IMBC in the presence of $V_{\rm bus}^{\rm ref}$ variations. At t = 0.05 s, $V_{\rm bus}^{\rm ref}$ steps up from 300 to 400 V, and then further rises to 500 V at t = 0.07 s. It can be seen that $v_{\rm bus}$ tightly tracks its new references within 5.0 ms. Meanwhile, the three-phase inductor current balance is also held during the output voltage reference changes. Meanwhile, the three-phase inductor currents and terminal voltages of the switched capacitors are also balanced well when the output voltage reference changes.

4) Robustness of Parameter Uncertainties: Fig. 10 shows the output voltage responses of the IMBC with the proposed strategy against the circuit parameter uncertainties. In this simulation, four groups of inductance and capacitance, Case 1: $L_i = 1.2L$,

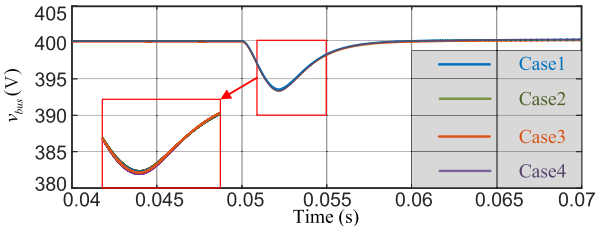

Fig. 10. Output voltage responses considering the circuit parameter uncertainties of the IMBC.

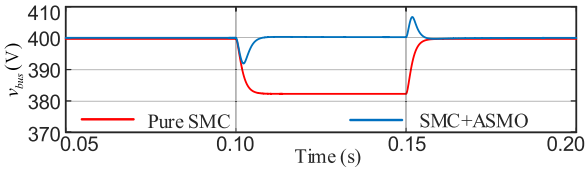

Fig. 11. Effectiveness of the ASMO.

$C_j = 1.1C$, Case 2: $L_i = 1.2L$, $C_j = 0.9C$, Case 3: $L_i = 0.8L$, $C_j = 1.1C$, Case 4: $L_i = 0.8L$, $C_j = 0.9C$, ($i = 1, 2, 3$, $j = 1, 2$.) are considered. It can be seen that the proposed controller provides almost the same voltage responses regardless of the circuit parameter deviations. Hence, the proposed controller has strong robustness against the circuit parameter uncertainties.

5) Effectiveness of the ASMO: To verify the effectiveness of the ASMO, the comparative simulation results of the IMBC, respectively, controlled by the pure SMC and ASMO-based SMC are shown in Fig. 11. In this case, the CPL increases from 2.0 to 6.0 kW at 0.10 s while returning 2.0 kW at 0.15 s. Due to the absence of ASMOs, the pure SMC is designed based on the references x_1^{ref} and x_2^{ref}, instead of $\hat{x}_1^{\text{ref}}$ and $\hat{x}_2^{\text{ref}}$, the condition of $u_1 + x_2^{\text{ref}} = 0$ will be destroyed when the CPL is changed to 6.0 kW. Thus, the output voltage of the pure SMC-regulated IMBC drops to 382 V, while the output voltage of the IMBC controlled by the proposed ASMO-based SMC can accurately track the desired voltage reference. This simulation result shows the effectiveness of the ASMO.

C. Comparison With the PI Controller

To show the superiority of the proposed controller in terms of regulating IMBC-based dc MG with CPL, a comparative study involving the proposed controller and a PI controller is carried out. In this study, only the CPL is adopted in the dc MG to simulate the worst system stability condition. To achieve a fair comparison, gains of the PI controller are fine-tuned to achieve similar system transient responses to the proposed controller.

Fig. 12 shows the dynamic responses of the system controlled by the proposed controller and the fine-turned PI controller, respectively. It can be found that, although both controllers provide similar dc bus voltage transient responses during the CPL power changes, the PI controller fails to stabilize the system under the heavy CPL case. The results imply that the system regulated by the proposed controller holds a wider stability margin compared to that using the PI controller.

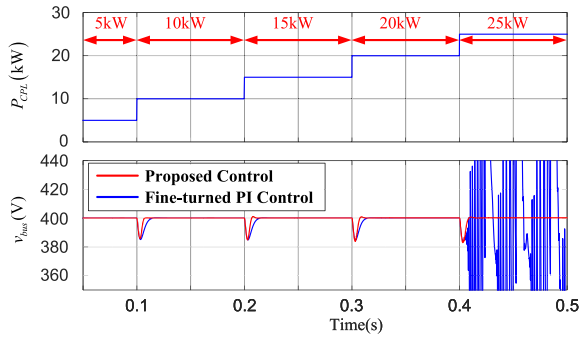

Fig. 12. DC bus voltage of the IMBC in the presence of large CPL changes.

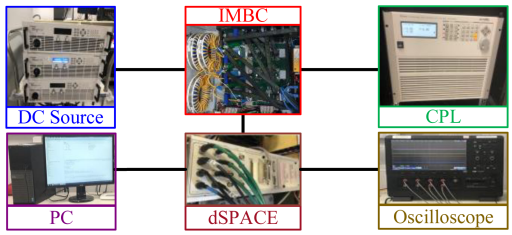

Fig. 13. Hardware experimental platform.

V. Experimental Results

To validate the effectiveness of the proposed controller in practical applications, an experimental platform, as shown in Fig. 13, is built up. In the following experiment verifications, a three-phase two-level IMBC experimental prototype is adopted. The dc voltage source is connected to the dc bus by the interfacing IMBC and the Chrome programmable electronic load is programmed to operate as a CPL. The control algorithm in Fig. 4 is implemented using MATLAB/Simulink and then coded into dSPACE real-time control card to generate corresponding PWM signals and then drive the power switches in the IMBC model.

In the following figures of experimental results (see Fig. 14), E represents the input voltage; v_{bus}, v_{c1}, and v_{c2} indicate the dc bus voltage and output side capacitor voltages; i_{L1}, i_{L2}, and i_{L3} are the inductor currents. To show the advantages of the proposed controller in the worst stability condition, the experiments are conducted using pure CPL without resistive loads.

1) CPL Variations: Fig. 14(a) shows experimental results of the system in the presence of CPL power variations. Initially, a 2 kW-CPL is connected to the dc bus. At $t = 0.76$ s and $t = 1.46$ s, the CPL power steps to 4 and 6 kW, respectively. As seen from the figure, the dc bus voltage rapidly returns to its reference 400 V (within 8 ms) with negligible steady-state error after each CPL power variation. In addition, the three-phase inductor currents are balanced successfully at both the transient and steady states. Meanwhile, the waveforms of v_{c1} and v_{c2} imply the self-voltage-balancing between the capacitors is achieved.

2) Input Voltage Variations: Fig. 14(b) shows the experimental results of the studied system under the input voltage variations. The CPL in the power of 2.5 kW is used in this experiment case. At $t = 0.76$ s, the input voltage drops from 100 to 50 V.

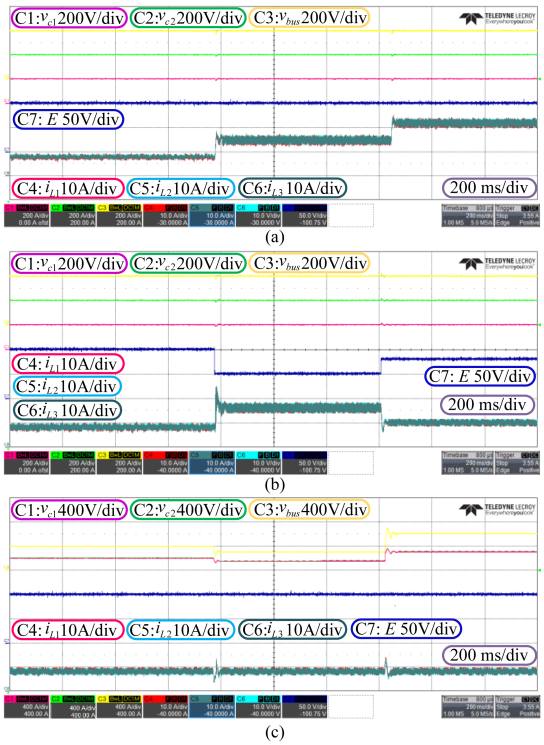

Fig. 14. Dynamic responses of the IMBC in the presence of (a) CPL changes, (b) input voltage changes, and (c) output voltage reference changes.

It can be seen that the impact of input voltage disturbance is eliminated within 20 ms. Then, the input voltage steps to 80 V at $t = 1.42$ s. Again, the dc bus voltage is stabilized at its reference of 400 V after a short transient period (within 24 ms). Note that the self-voltage balancing of the capacitors and the phase current balancing of the inductors are held during the input voltage variations.

3) Output Voltage Reference Variations: Fig. 14(c) shows the experimental results of the studied system in the presence of output voltage reference variations. Also, the 2.5 kW-CPL is used in this experiment. When the output voltage reference drops from 400 to 300 V at $t = 0.76$ s, the dc bus voltage rapidly tracks its new reference value within 30 ms. At $t = 1.44$ s, the output voltage reference jumps to 600 V. Similarly, the dc bus voltage is regulated to its new reference with negligible steady-state error and short settling time.

According to the experimental results, the proposed ASMO-based SMC guarantees the large-signal stability of the IMBC-based dc MG with CPL, and both the fast system transient performance and dc bus voltage tracking are achieved. In addition, the features of self-voltage balancing in capacitors and phase current balancing in inductors are ensured in the presence of various large-signal disturbances.

VI. Conclusion

In this article, an ASMO-based SMC is proposed to guarantee the large-signal stability of the IMBC interfaced dc MG system with high penetration of CPLs. To simplify the controller design and system analysis, a generalized reduced-order model of the M-phase N-level IMBC is derived. Based on this model, an ASMO is adopted to estimate the disturbances without knowing their boundaries, which contributes to improving the system's dynamic performance and alleviating the chattering problem of the SMC. In addition, the self-voltage balancing and phase current balancing of the interface converter are achieved. The effectiveness of the proposed control law is verified by simulation and experimental results. It is worth noting that the proposed control scheme is also feasible for many other converter topologies.

References

[1] Y. Gui, R. Han, J. M. Guerrero, J. C. Vasquez, B. Wei, and W. Kim, "Large-signal stability improvement of DC-DC converters in DC microgrid," *IEEE Trans. Energy Convers.*, vol. 36, no. 3, pp. 2534–2544, Sep. 2021.

[2] Z. Wang, P. Wang, B. Li, X. Ma, and P. Wang, "A bidirectional DC–DC converter with high voltage conversion ratio and zero ripple current for battery energy storage system," *IEEE Trans. Power Electron.*, vol. 36, no. 7, pp. 8012–8027, Jul. 2021.

[3] M. S. Bhaskar, D. J. Almakhles, S. Padmanaban, F. Blaabjerg, U. Subramaniam, and D. M. Ionel, "Analysis and investigation of hybrid DC–DC non-isolated and non-inverting NX interleaved multilevel boost converter (NX-IMBC) for high voltage step-up applications: Hardware implementation," *IEEE Access*, vol. 8, pp. 87309–87328, 2020.

[4] B. A. Miwa, D. M. Otten, and M. Schlecht, "High efficiency power factor correction using interleaving techniques," in *Proc. 7th Annu. Appl. Power Electron. Conf. Expo.*, 1992, pp. 557–568.

[5] J. C. Rosas-Caro, J. M. Ramirez, F. Z. Peng, and A. Valderrabano, "A DC–DC multilevel boost converter," *IET Power Electron.*, vol. 3, no. 1, pp. 129–137, 2010.

[6] M. Gutierrez, P. A. Lindahl, and S. B. Leeb, "Constant power load modeling for a programmable impedance control strategy," *IEEE Trans Ind. Electron.*, vol. 69, no. 1, pp. 293–301, Jan. 2022.

[7] W. Yuan, Y. Wang, D. Liu, F. Deng, and Z. Chen, "Impacts of inductor nonlinear characteristic in multiconverter microgrids: Modeling, analysis, and mitigation," *IEEE Trans. Emerg. Sel. Topics Power Electron.*, vol. 8, no. 4, pp. 3333–3347, Dec. 2020.

[8] H. Wang, X. Ge, and Y.-C. Liu, "An active damping stabilization scheme for the suppression of the dc-link oscillation in metro traction drive system," *IEEE Trans. Ind. Appl.*, vol. 54, no. 5, pp. 5113–5123, Sep./Oct. 2018.

[9] M. Wu and D. D.-C. Lu, "A novel stabilization method of LC input filter with constant power loads without load performance compromise in DC microgrids," *IEEE Trans. Ind. Electron.*, vol. 62, no. 7, pp. 4552–4562, Jul. 2015.

[10] X. Lu, K. Sun, J. M. Guerrero, J. C. Vasquez, L. Huang, and J. Wang, "Stability enhancement based on virtual impedance for DC microgrids with constant power loads," *IEEE Trans. Smart Grid*, vol. 6, no. 6, pp. 2770–2783, Nov. 2015.

[11] H. G. Narm, S. Eren, and M. K. Ghartemani, "A robust controller with integrated plant dynamics for constant power loads in DC microgrid," *IEEE Trans. Power Electron.*, vol. 38, no. 4, pp. 4419–4429, Apr. 2023.

[12] X. Zhang, Q.-C. Zhong, V. Kadirkamanathan, J. He, and J. Huang, "Source-side series-virtual-impedance control to improve the cascaded system stability and the dynamic performance of its source converter," *IEEE Trans Power Electron.*, vol. 34, no. 6, pp. 5854–5866, Jun. 2019.

[13] M. A. Hassan, E.-P. Li, X. Li, T. Li, C. Duan, and S. Chi, "Adaptive passivity-based control of DC–DC buck power converter with constant power load in DC microgrid systems," *IEEE Trans. Emerg. Sel. Topics Power Electron.*, vol. 7, no. 3, pp. 2029–2040, Sep. 2019.

[14] Q. Xu, Y. Yan, C. Zhang, T. Dragicevic, and F. Blaabjerg, "An offset-free composite model predictive control strategy for DC/DC buck converter feeding constant power loads," *IEEE Trans. Power Electron.*, vol. 35, no. 5, pp. 5331–5342, May 2020.

[15] Z. Karami, Q. Shafiee, Y. Khayat, M. Yaribeygi, T. Dragičević, and H. Bevrani, "Decentralized model predictive control of DC microgrids with constant power load," *IEEE Trans. Emerg. Sel. Topics Power Electron.*, vol. 9, no. 1, pp. 451–460, Feb. 2021.

[16] S. Singh, D. Fulwani, and V. Kumar, "Robust sliding-mode control of DC/DC boost converter feeding a constant power load," *IET Power Electron.*, vol. 8, no. 7, pp. 1230–1237, 2015.

[17] D. Peng, M. Huang, J. Li, J. Sun, X. Zha, and C. Wang, "Large-signal stability criterion for parallel-connected DC–DC converters with current source equivalence," *IEEE Trans. Circuits Syst. II: Exp. Briefs*, vol. 66, no. 12, pp. 2037–2041, Dec. 2019.
[18] Q. Xu, C. Zhang, C. Wen, and P. Wang, "A novel composite nonlinear controller for stabilization of constant power load in DC microgrid," *IEEE Trans. Smart Grid*, vol. 10, no. 1, pp. 752–761, Jan. 2019.
[19] P. Lin, C. Zhang, X. Zhang, H. H. C. Iu, Y. Yang, and F. Blaabjerg, "Finite-time large signal stabilization for high power DC microgrids with exact offsetting of destabilizing effects," *IEEE Trans. Ind. Electron.*, vol. 68, no. 5, pp. 4014–4026, May 2021.
[20] X. Wang et al., "Toward balancing dynamic performance and system stability for dc microgrids: A new decentralized adaptive control strategy," *IEEE Trans. Smart Grid*, vol. 13, no. 5, pp. 3439–3451, Sep. 2022.
[21] Z. Liu et al., "Further results on Newton-Raphson method in feasible power-flow for DC distribution networks," *IEEE Trans. Power Del.*, vol. 37, no. 2, pp. 1348–1351, Apr. 2022.
[22] P. Lin, W. Jiang, J. Wang, D. Shi, C. Zhang, and P. Wang, "Toward large-signal stabilization of floating dual boost converter-powered DC microgrids feeding constant power loads," *IEEE Trans. Emerg. Sel. Topics Power Electron.*, vol. 9, no. 1, pp. 580–589, Feb. 2021.
[23] C. A. Villarreal-Hernandez, J. C. Mayo-Maldonado, J. E. Valdez-Resendiz, and J. C. Rosas-Caro, "Modeling and control of an interleaved DC-DC multilevel boost converter," in *Proc. IEEE 18th Workshop Control Model. Power Electron.*, 2017, vol. 1, pp. 1–6.
[24] H. Sira-Ramirez and M. Ilic-Spong, "Exact linearization in switched-mode DC-to-DC power converters," *Int. J. Control*, vol. 50, no. 2, pp. 511–524, 1989.
[25] J. Han, "From PID to active disturbance rejection control," *IEEE Trans. Ind. Electron.*, vol. 56, no. 3, pp. 900–906, Mar. 2009.
[26] C. Edwards and Y. B. Shtessel, "Adaptive continuous higher order sliding mode control," *Automatica*, vol. 65, pp. 183–190, 2016.
[27] J. Yang, S. Li, J. Su, and X. Yu, "Continuous nonsingular terminal sliding mode control for systems with mismatched disturbances," *Automatica*, vol. 49, no. 7, pp. 2287–2291, 2013.
[28] S. Li and Y.-P. Tian, "Finite-time stability of cascaded time-varying systems," *Int. J. Control*, vol. 80, no. 4, pp. 646–657, 2007.
[29] J.-C. Wu, H.-L. Jou, P.-H. Huang, and I.-H. Chiu, "Current balancing control for an interleaved boost power converter," *Int. J. Electron.*, vol. 106, no. 10, pp. 1567–1582, 2019.
[30] R. Wang, Q. Sun, C. Sun, H. Zhang, Y. Gui, and P. Wang, "Vehicle-vehicle energy interaction converter of electric vehicles: A disturbance observer based sliding mode control algorithm," *IEEE Tran. Veh. Technol.*, vol. 70, no. 10, pp. 9910–9921, Oct. 2021.

Wentao Jiang (Member, IEEE) received the B.Eng. degree from the Xi'an University of Technology, Xi'an, China, the M.Sc. and Ph.D. degrees from the National University of Singapore, Singapore, in 2011, 2013, and 2018, respectively, all in electrical engineering.

He is currently an Associate Professor with the College of Automation, Northwestern Polytechnical University, Xi'an, China. From 2018 to 2020, he was a Research Fellow with Energy Research Institute @ NTU (ERI@N), Singapore. His research focuses on modeling and control of the dc/dc converters in dc microgrid.

Zhishuang Wang received the B.S. degree from China Three Gorges University, Yichang, China, in 2016, and the Ph.D. degree from Tianjin University, Tianjin, China, in 2022, both in electrical engineering.

Her research interests include dc–dc converters and vehicle-to-grid.

Xiangke Li (Member, IEEE) received the B.Eng. and Ph.D. degrees in electrical engineering from Northwestern Polytechnical University, Xi'an, China, in 2016 and 2021, respectively.

He is currently a Professor with College of Automation, Northwestern Polytechnical University. From 2021 to 2024, he was a Postdoctoral Scholar with the Department of Electrical and Electronic Engineering, The Hong Kong Polytechnic University, Hong Kong, China. His research interests include power-electronized microgrids, and electrical power system stability analysis.

Rui Ma (Member, IEEE) received the bachelor's and master's degrees in electrical engineering from Northwestern Polytechnical University (NPU), Xi'an, China, in 2013 and 2016, respectively, and the Ph.D. degrees in electrical engineering from the University of Technology of Belfort-Montbéliard, Belfort, France, in 2018, and NPU, in 2019.

He is currently an Associate Professor with the School of Automation, NPU. His research interests include fuel cell modeling, fuel cell applications, real-time simulation systems, and machine learning.

Dr. Ma was a Member for the Technical Committee on Transportation Electrification of the IEEE IES, and the Special Session Chair of 45th, 46th, and 47th IEEE IECON. He is an Associate Editor for IEEE IES Industrial Electronics Technology News and a Distinguish Reviewer for IEEE TRANSACTIONS ON INDUSTRIAL ELECTRONICS.

Sunhua Huang received the Ph.D. degree in electrical engineering from Shanghai Jiao Tong University, Shanghai, China, in 2022.

From 2022 to 2023, he was an Assistant Professor with the School of Mechatronic Engineering and Automation, Shanghai University, Shanghai, China. He is currently a Postdoctoral Fellow with Hong Kong Polytechnic University, Hong Kong, China. His research interests include power system stability control, renewable energy, and ac/dc microgrids.

Chaoyu Dong received the B.S. degree in electrical engineering from Tianjin University, Tianjin, China, in 2013.

He is currently with the Agency for Science, Technology and Research and Nanyang Technological University, Singapore. His research interests include energy information system stability and intelligent management.

Xiaohua Wu received the B.S. and M.S. degrees in electrical engineering, and the Ph.D. degree in control theory and control engineering from Northwestern Polytechnical University (NPU), Xi'an, China, in 1991, 1994, and 2004, respectively.

In 1994, she joined the School of Automation, NPU, where she is currently a Professor. Her research interests include power quality, modeling and control of power converters, and distributed generation systems.